

Optical analogues to the Kerr–Newman black hole

R. A. Tinguely[†] and Andrew P. Turner[‡]

[†]*Plasma Science and Fusion Center
Massachusetts Institute of Technology
77 Massachusetts Avenue
Cambridge, MA 02139, USA*

[‡]*Center for Theoretical Physics
Massachusetts Institute of Technology
77 Massachusetts Avenue
Cambridge, MA 02139, USA*

September 1, 2022

Abstract

Optical analogues to black holes conveniently allow the investigation of general relativity in a laboratory setting. Previous works have considered analogues to Schwarzschild black holes in an isotropic coordinate system; the major drawback of this approach is that required material properties diverge at the horizon. In this paper, we present the dielectric permittivity and permeability tensors ϵ, μ that exactly reproduce the Kerr–Newman metric, as well as the gradient-index material that reproduces the equatorial Kerr–Newman null geodesics. Of particular interest, the radial profile of the scalar refractive index $n(R)$ is finite along all trajectories except at the point of rotation reversal for counter-rotating null geodesics. Importantly, construction of these optical black holes is feasible even with available ordinary materials: $n(R)$ can be approximated with concentric circular annuli, with $n(R) \lesssim 6$. A finite-difference frequency-domain solver of Maxwell’s equations is used to simulate the light trajectories around a variety of Kerr–Newman black holes. For reasonably sized experimental systems, ray tracing confirms that null geodesics can be well-approximated in the lab, even when allowing for imperfect construction of the optical black hole and experimental error.

1 Introduction

In recent years, there has been a great amount of interest in precisely controlling the electromagnetic response of artificial materials. By introducing subwavelength structural features, the permittivity and permeability tensors of the medium can be tuned to exhibit a wide range of interesting and useful phenomena, such as cloaking [1–7], negative refraction [1, 8, 9], and subwavelength microscopy with superlenses [10–13].

Transformation optics [1, 2, 14–18] uses optical materials to implement coordinate transformations between a physical space and a virtual “electromagnetic space,” via the formal equivalence between Maxwell’s equations in curved spacetime and those in flat spacetime within a corresponding bianisotropic medium [19–23]. Among other applications, this allows one to build optical analogues to gravitational systems [24–43]. In particular, there has been a fair amount of interest in reproducing the metrics of black holes [44–47]. The desired metric can be reproduced exactly within a fully bianisotropic material; if one simply wishes to reproduce the null geodesics of the metric, however, it is much simpler to use an appropriately designed gradient-index material that is easier to construct experimentally.

In this paper, we discuss the bianisotropic and gradient-index materials that imitate the exterior Kerr–Newman black hole solution. In [Section 2](#), we first carry out the analysis for optical systems reproducing

[†]rating at mit.edu, [‡]apturner at mit.edu

the geodesics of the Schwarzschild black hole. We recover the familiar results for the permittivity and permeability tensors and scalar refractive index reproducing the metric in isotropic coordinates, as well as the permittivity and permeability tensors reproducing the metric in the Schwarzschild coordinates [20, 45, 46, 48]. We then present the scalar index that reproduces the null geodesics for Schwarzschild coordinates, which, by comparison with the isotropic result, has the significant experimental benefit of remaining finite all the way to the horizon. In Section 3, we carry out these same analyses for the Kerr–Newman metric in Boyer–Lindquist coordinates, reproducing the metric exactly within a fully bianisotropic material [23], and finding the scalar index required to reproduce the null geodesics. In Section 4, we use finite-difference frequency-domain simulations of systems that approximate the gradient-index solutions of the Schwarzschild and Kerr–Newman black holes with concentric spherical shells of constant index, and use ray tracing to perform an analysis of the error sensitivity of such systems. These analyses demonstrate that these approximate gradient-index systems, which are far simpler to construct than true gradient-index systems or full bianisotropic media, can adequately reproduce null geodesics and are forgiving to fabrication and experimental error for reasonable geodesics. As such, they are practical tabletop analogues for charged and/or rotating black holes.

Throughout this paper we use Gaussian Planck units, with $c = \hbar = G = 4\pi\epsilon_0 = 1$. Greek indices range over temporal and spatial coordinates, e.g., $\mu = 0, \dots, 3$, while Roman indices range over only spatial coordinates, e.g., $i = 1, \dots, 3$. We use uppercase Greek and Roman letters to indicate variables related to the optical system, while we use lowercase letters to indicate variables related to the spacetime metric it is replicating. We refer to these respectively as “real space” and “spacetime” variables. We typically use hats to indicate the dimensionless versions of variables.

When we map spacetime coordinates onto real space coordinates, we always do so by equating the dimensionless coordinates. Spacetime variables are dedimensionalized via multiplication by the appropriate power of the black hole mass M . Real space dimensionless variables are then dimensionalized by a convenient length scale for construction. Using this matching of coordinates allows one to easily keep track of the relationship between real space coordinates and the spacetime coordinates they represent.

2 The Schwarzschild black hole

We will begin by studying the Schwarzschild black hole and various optical analogues thereof. The Schwarzschild metric describes the spacetime geometry of a static, uncharged black hole of mass M , and is given in dimensionless Schwarzschild coordinates $\hat{s}, \hat{t}, \rho, \theta, \phi$ (related to the usual dimensionful quantities via $s = M\hat{s}$, $t = M\hat{t}$, $r = M\rho$) by [49]

$$d\hat{s}^2 = -\left(1 - \frac{2}{\rho}\right) d\hat{t}^2 + \left(1 - \frac{2}{\rho}\right)^{-1} d\rho^2 + \rho^2(d\theta^2 + \sin^2\theta d\phi^2). \quad (1)$$

Making the coordinate transformation $\rho = \tilde{\rho}\left(1 + \frac{1}{2\tilde{\rho}}\right)^2$, the Schwarzschild metric Eq. (1) can be written in the form [49]

$$d\hat{s}^2 = -\frac{\left(1 - \frac{1}{2\tilde{\rho}}\right)^2}{\left(1 + \frac{1}{2\tilde{\rho}}\right)^2} d\hat{t}^2 + \left(1 + \frac{1}{2\tilde{\rho}}\right)^4 (d\hat{x}^2 + d\hat{y}^2 + d\hat{z}^2), \quad (2)$$

where the spacetime isotropic coordinates $(\hat{x}, \hat{y}, \hat{z})$ are related to the transformed Schwarzschild coordinates $(\tilde{\rho}, \theta, \phi)$ via the transformation from Cartesian to spherical coordinates.

2.1 Isotropic coordinates

We begin by replicating the metric in isotropic coordinates Eq. (2), in order to make contact with existing literature.

As discussed in [15, 19], there is a formal equivalence between the equations of electrodynamics in a curved spacetime and those in flat space in a macroscopic medium. Specifically, the behavior of light in a curved spacetime background described by metric $g_{\mu\nu}$ is reproduced in flat space within an impedance-matched

bianisotropic medium with permittivity ϵ^{ij} , permeability μ^{ij} , and magnetoelectric coupling α_i given by

$$\epsilon^{ij} = \mu^{ij} = -\frac{\sqrt{-\det g}}{g_{00}\sqrt{\det \gamma}}g^{ij}, \quad \alpha_i = \frac{g_{0i}}{g_{00}\sqrt{\det \gamma}}, \quad (3)$$

where γ_{ij} is the three-dimensional metric tensor of the real space coordinate system in which we construct the medium, onto which we map the spatial components g_{ij} . Here, g and γ denote the determinants of $g_{\mu\nu}$ and γ_{ij} , respectively. The macroscopic fields \mathbf{D}, \mathbf{H} are related to the microscopic fields \mathbf{E}, \mathbf{B} via

$$\mathbf{D} = \epsilon \mathbf{E} + \boldsymbol{\alpha} \times \mathbf{H}, \quad \mathbf{B} = \mu \mathbf{H} - \boldsymbol{\alpha} \times \mathbf{E}. \quad (4)$$

Using Eq. (3) to map the dimensionless spacetime isotropic coordinates $(\hat{x}, \hat{y}, \hat{z})$ onto the corresponding dimensionless real space Cartesian coordinates $(\hat{X}, \hat{Y}, \hat{Z})$ (and thus mapping the dimensionless spacetime isotropic radial coordinate $\tilde{\rho}$ onto the dimensionless real space radial coordinate P), we find that the behavior of light in the Schwarzschild metric Eq. (1) is reproduced in flat space within a medium described by

$$\epsilon^{ij} = \mu^{ij} = \frac{(2P+1)^3}{4P^2(2P-1)} \mathbb{1}^{ij}, \quad i, j \in \{\hat{X}, \hat{Y}, \hat{Z}\}. \quad (5)$$

This result is well-established in the literature [20, 45, 46, 48].

In this case, the medium is isotropic, and the scalar index can be read off immediately from Eq. (5) as

$$n(P) = \frac{(2P+1)^3}{4P^2(2P-1)}. \quad (6)$$

This solution has the benefit that there is a single scalar index that reproduces all geodesics, and the material is isotropic (though still inhomogeneous) and thus easier to construct experimentally. However, this refractive index diverges approaching the horizon, i.e., as $P \rightarrow \frac{1}{2}$, so it is not useful for investigating geodesics in the vicinity of the horizon.

2.2 Schwarzschild coordinates

As before, we use Eq. (3) to map the dimensionless spacetime Schwarzschild coordinates (ρ, θ, ϕ) (now with the Schwarzschild radial coordinate ρ rather than the isotropic radial coordinate $\tilde{\rho}$) onto the corresponding dimensionless real space spherical coordinates (P, Θ, Φ) , yielding

$$\epsilon^{ij} = \mu^{ij} = \begin{pmatrix} 1 & 0 & 0 \\ 0 & \frac{1}{P(P-2)} & 0 \\ 0 & 0 & \frac{\csc(\Theta)^2}{P(P-2)} \end{pmatrix}, \quad i, j \in \{P, \Theta, \Phi\}. \quad (7)$$

This same system is described in dimensionless real space Cartesian coordinates $(\hat{X}, \hat{Y}, \hat{Z})$ by

$$\epsilon^{ij} = \mu^{ij} = \frac{1}{P^2(2-P)} \begin{pmatrix} 2\hat{X}^2 - P^3 & 2\hat{X}\hat{Y} & 2\hat{X}\hat{Z} \\ 2\hat{X}\hat{Y} & 2\hat{Y}^2 - P^3 & 2\hat{Y}\hat{Z} \\ 2\hat{X}\hat{Z} & 2\hat{Y}\hat{Z} & 2\hat{Z}^2 - P^3 \end{pmatrix} = \frac{2P^i P^j - P^3 \mathbb{1}^{ij}}{P^2(2-P)}, \quad i, j \in \{\hat{X}, \hat{Y}, \hat{Z}\}, \quad (8)$$

where $P^i = (\hat{X}, \hat{Y}, \hat{Z})$ and the dimensionless real space Cartesian coordinates $(\hat{X}, \hat{Y}, \hat{Z})$ are related to the real space spherical coordinates (P, Θ, Φ) in the usual way. This result matches those presented in [45, 46].

If we only wish to reproduce the trajectories of light in the Schwarzschild metric (and not the proper polarizations), then a radially varying scalar index $n(P)$ is sufficient. In Schwarzschild coordinates, we will find that the radial profile depends on the initial conditions. We consider null geodesics of the metric Eq. (1); all such geodesics are planar, and so the spherical symmetry allows us to take $\theta = \pi/2$ without loss of generality. Such null geodesics of the Schwarzschild metric are parametrized by a conserved energy at infinity, $\varepsilon = (1 - \frac{2M}{r}) \frac{dt}{d\sigma}$, and the conserved angular momentum, $\ell = r^2 \frac{d\phi}{d\sigma}$, with σ the affine parameter of

the geodesic. Dedimensionalizing these parameters via $\ell = M\hat{\ell}$ and $\sigma = M\hat{\sigma}$ (note that the energy is already dimensionless, $\hat{\varepsilon} = \varepsilon$), null geodesics satisfy the geodesic equation [49]

$$-\hat{\varepsilon}^2 + \left(\frac{d\rho}{d\hat{\sigma}}\right)^2 + \left(1 - \frac{2}{\rho}\right)\frac{\hat{\ell}^2}{\rho^2} = 0. \quad (9)$$

Combining this equation with $\left(\frac{d\phi}{d\hat{\sigma}}\right)^2 = \hat{\ell}^2/\rho^4$ yields

$$\frac{d\phi}{d\rho} = \pm \left(\frac{\hat{\varepsilon}^2}{\hat{\ell}^2}\rho^4 - \rho^2 + 2\rho\right)^{-1/2}. \quad (10)$$

We then make use of the spacetime impact parameter $\hat{b}(\rho) = \rho \sin \beta$, where β is defined by the relation

$$\rho \frac{d\phi}{d\rho} = -\tan \beta. \quad (11)$$

Plugging this relation into Eq. (10) and making the sign choice consistent with our definition of β , we find that

$$\hat{b}(\rho) = \left(\hat{b}_\infty^{-2} + 2\rho^{-3}\right)^{-1/2}, \quad (12)$$

where we have defined $\hat{b}_\infty = \hat{\ell}/\hat{\varepsilon}$.

Fermat's principle relates the real space impact parameter and index of refraction by

$$n(P) \propto \hat{B}(P)^{-1}. \quad (13)$$

Equation (12) is then taken as input to Eq. (13) by equating the spacetime coordinates (ρ, ϕ) with the real space coordinates (P, Φ) , which also equates the dimensionless spacetime impact parameter \hat{b} with the dimensionless real space impact parameter \hat{B} . This yields

$$n(P) \propto \hat{B}(P)^{-1} = \sqrt{\hat{b}_\infty^{-2} + 2P^{-3}}. \quad (14)$$

This solution has a number of noteworthy features. First, the radial profile depends on the initial condition \hat{b}_∞ , which is related to initial angle β and initial radius P_0 by

$$\hat{b}_\infty^2 = \frac{P_0^2}{\csc^2 \beta_0 - 2P_0^{-1}}. \quad (15)$$

This is somewhat inconvenient for experimental application, as it means that a different apparatus must be constructed for each family of geodesics; to address this, one could in principle construct a cylinder, where \hat{b}_∞ varies along the cylinder axis and each 2D slice recreates the corresponding family of null geodesics. A significant benefit of this coordinate system, however, is that $n(P)$ approaches a finite value as $P \rightarrow 2$ so long as $\hat{b}_\infty \neq 0$, which means that geodesics can be studied in the vicinity of the event horizon, in contrast to the solution Eq. (6). The constant of proportionality in Eq. (14) allows us to tune the scalar index at the initial P_0 to the most feasible value for construction.

Finally, note that we can relate conserved quantities $\hat{\varepsilon}, \ell$ in spacetime to \mathcal{E}, L in real space in the following way: In flat space, a photon with frequency f and wavelength λ has energy $\mathcal{E} = 2\pi f$ and angular momentum $L = 2\pi B/\lambda$, with B the dimensionful real space impact parameter. Thus, $L/\mathcal{E}R_S = n\hat{B}/2 = \text{constant}$. Setting $n = 1$ at $P \rightarrow \infty$ in Eq. (14) and equating the real space and spacetime dimensionless impact parameters, $\hat{B} = \hat{b}$, yields $L/\mathcal{E}R_S = \ell/\varepsilon r_S$. Here, $r_S = 2M$, and R_S is the real space radius onto which r_S is mapped.

3 The Kerr–Newman black hole

We now apply the same approaches to investigate optical analogues of the Kerr–Newman black hole, of which the Kerr, Reissner–Nordström, and Schwarzschild results are special cases. We will restrict our attention to equatorial null geodesics.

The Kerr–Newman metric describes the spacetime geometry surrounding a black hole of mass M , angular momentum per unit mass $a = J/M$, electric charge Q , and magnetic charge Q_m . Dedimensionalizing the quantities via $a = M\hat{a}$, $Q = M\hat{Q}$, $Q_m = M\hat{Q}_m$, the metric is given in dimensionless Boyer–Lindquist coordinates by [49]

$$d\hat{s}^2 = \hat{\Sigma} \left(\frac{d\rho^2}{\hat{\Delta}} + d\theta^2 \right) - \frac{\hat{\Delta}}{\hat{\Sigma}} (d\hat{t} - \hat{a} \sin^2 \theta d\phi)^2 + \frac{\sin^2 \theta}{\hat{\Sigma}} [(\rho^2 + \hat{a}^2) d\phi - \hat{a} d\hat{t}]^2. \quad (16)$$

where

$$\begin{aligned} \hat{\Sigma} &= \rho^2 + \hat{a}^2 \cos^2 \theta, \\ \hat{\Delta} &= \rho^2 - 2\rho + \hat{a}^2 + \rho_Q^2, \\ \rho_Q^2 &= \hat{Q}^2 + \hat{Q}_m^2. \end{aligned} \quad (17)$$

Here, M is the total mass-equivalent, which contains contributions from the irreducible mass, the rotational energy, and the Coulomb energy of the black hole [50].

We use Eq. (3) to map the dimensionless spacetime coordinates (ρ, θ, ϕ) onto the dimensionless real space coordinates (P, Θ, Φ) , as before, yielding

$$\epsilon^{ij} = \mu^{ij} = \begin{pmatrix} \frac{\hat{\Delta}}{\hat{\Delta} - \hat{a}^2} & 0 & 0 \\ 0 & \frac{1}{\hat{\Delta} - \hat{a}^2} & 0 \\ 0 & 0 & \frac{1}{\hat{\Delta}} \end{pmatrix}, \quad \alpha_i = \begin{pmatrix} 0 \\ 0 \\ \hat{a} \left(\frac{1}{\hat{\Delta} - \hat{a}^2} - \frac{1}{P^2} \right) \end{pmatrix}, \quad (18)$$

where $\hat{\Delta}$ should now be interpreted as a function of P . The Kerr–Newman metric is exactly reproduced in flat space within a medium with these properties [23]. There is a subtlety here—although the radial and azimuthal components P, Θ appear to diverge at the ergosphere $\hat{\Delta} = \hat{a}^2$, this is a spurious divergence. As discussed in [23, 51, 52], the physically relevant covariant quantity is their tensor χ , which relates the macroscopic and microscopic fields. This quantity diverges only at the horizon $\hat{\Delta} = 0$.

As before, we can also replicate null geodesics of the Kerr–Newman metric using only a scalar index. Null geodesics with initial position and velocity vectors lying within the plane $\theta = \pi/2$ will remain within this plane; we restrict our attention to such equatorial geodesics. As in the Schwarzschild case, these geodesics are parametrized by the dimensionless conserved energy at infinity and conserved angular momentum, given in this case by

$$\begin{aligned} \hat{\epsilon} &= \left(1 - \frac{2}{\rho} + \frac{\rho_Q^2}{\rho^2} \right) \frac{d\hat{t}}{d\hat{\sigma}} + \left(\frac{2\hat{a}}{\rho} - \frac{\rho_Q^2 \hat{a}}{\rho^2} \right) \frac{d\phi}{d\hat{\sigma}}, \\ \hat{\ell} &= - \left(\frac{2\hat{a}}{\rho} - \frac{\rho_Q^2 \hat{a}}{\rho^2} \right) \frac{d\hat{t}}{d\hat{\sigma}} + \left(\rho^2 + \hat{a}^2 + \frac{2\hat{a}^2}{\rho} - \frac{\rho_Q^2 \hat{a}^2}{\rho^2} \right) \frac{d\phi}{d\hat{\sigma}}. \end{aligned} \quad (19)$$

The geodesic equations describing the equatorial motion are

$$\begin{aligned} \frac{d\phi}{d\hat{\sigma}} &= \frac{1}{\hat{\Delta}} \left[\left(1 - \frac{2}{\rho} + \frac{\rho_Q^2}{\rho^2} \right) \hat{\ell} + \left(\frac{2\hat{a}}{\rho} - \frac{\rho_Q^2 \hat{a}}{\rho^2} \right) \hat{\epsilon} \right], \\ \left(\frac{d\rho}{d\hat{\sigma}} \right)^2 &= \frac{[(\rho^2 + \hat{a}^2)^2 - \hat{a}^2 \hat{\Delta}] \hat{\ell}^2}{\rho^4} (\hat{b}_\infty^{-1} - \hat{V}_+) (\hat{b}_\infty^{-1} - \hat{V}_-), \end{aligned} \quad (20)$$

where

$$\hat{V}_\pm = \frac{\hat{a}(2\rho - \rho_Q^2) \pm \text{sgn}(\hat{\ell}) \rho^2 \sqrt{\hat{\Delta}}}{(\rho^2 + \hat{a}^2)^2 - \hat{a}^2 \hat{\Delta}}. \quad (21)$$

As before, we find the impact parameter $\hat{b}(\rho) = \rho \sin \beta$ by plugging Eq. (11) into $\frac{d\phi}{d\rho} = \frac{d\phi/d\hat{\sigma}}{d\rho/d\hat{\sigma}}$, which yields

$$\hat{b}(\rho) = \frac{\rho^2 \left[(\hat{\Delta} - \hat{a}^2) + (2\rho - \rho_Q^2) \hat{a} \hat{b}_\infty^{-1} \right]}{\sqrt{\rho^2 \left[(\hat{\Delta} - \hat{a}^2) + (2\rho - \rho_Q^2) \hat{a} \hat{b}_\infty^{-1} \right]^2 + \hat{\Delta}^2 \left[(\rho^2 + \hat{a}^2)^2 - \hat{a}^2 \hat{\Delta} \right] (\hat{b}_\infty^{-1} - \hat{V}_+) (\hat{b}_\infty^{-1} - \hat{V}_-)}}. \quad (22)$$

We proceed by equating spacetime coordinates (ρ, θ, ϕ) and real space coordinates (P, Θ, Φ) , which sets $\hat{B}(P) = \hat{b}(\rho = P)$. The scalar index for an optical Kerr–Newman black hole is again given by

$$n(P) \propto \hat{B}(P)^{-1}. \quad (23)$$

Unlike the Schwarzschild case, this scalar index is not always sufficient to fully reproduce the given family of Kerr–Newman geodesics. This can be seen immediately by noting that initially counter-rotating geodesics (those with $\hat{\ell}$ of opposite sign to \hat{a}) must turn around and become co-rotating before crossing into the ergosphere; such a reversal of the sign of $\frac{d\phi}{d\rho}$ is not possible with a finite (and positive) scalar index. This shortcoming manifests itself as a divergence of the scalar index; the outermost divergence occurs at radius

$$P_* = 1 - \hat{a}\hat{b}_\infty^{-1} + \sqrt{\left(1 - \hat{a}\hat{b}_\infty^{-1}\right)\left(1 - \hat{a}\hat{b}_\infty^{-1} - \rho_Q^2\right)}. \quad (24)$$

This pole is removable in the Schwarzschild and Reissner–Nordström cases. For rotating black holes, the divergence occurs at the point in the trajectory where the direction of rotation reverses, consistent with the above observation that a finite radially varying scalar index is insufficient to implement such a reversal. Thus, the pole only affects initially counter-rotating geodesics that enter the ergosphere.

4 Simulations of constructible optical black holes

Optical analogues to black holes are particularly useful if their constructions are realizable. In the following sections, we model optical black holes with radially varying scalar refractive indices $n(P)$, as given by Eqs. (14) and (23). For Schwarzschild (and many Kerr–Newman) black holes, $n(P)$ is maximal at the horizon. Because the impact parameter of light on the optical black hole must be less than or equal to the radius of the “edge” of the system, i.e., $\hat{B} \leq P_0$, it is found that $n(P) \leq c_0 n_0 P_0$, where $c_0 = \sqrt{31/108} \approx 0.54$ and $n_0 = n(P_0)$. Thus, the construction of an optical Schwarzschild black hole with $n_0 = 1$ and moderate $P_0 \leq 6$ is plausible and achievable with indices of refraction in the range of ordinary materials such as water, glass, and plastic; true gradient-index profiles of the form Eq. (14) could perhaps be achieved with metamaterials. As will be seen, many optical Kerr–Newman black holes are also constructible.

In this study, all optical black holes are modeled with dimensionless outer radius $P_0 = 6$. The system comprises either 16 or 21 concentric annuli, with the number depending on acceptable annulus thickness and the minimum modeled radius P_{\min} . The innermost and outermost annuli each have half the width of each interior annulus. The scalar index of each annulus is uniform, so that the simulated $n(P)$ profiles are piecewise functions, as shown in Figure 1. The values of n for the innermost and outermost annuli are taken as $n(P)$ at the minimum and maximum radii, respectively; the refractive index of an inner annulus is taken as the value of $n(P)$ at its center. Note, in Figure 1, that the real space scale ($R = 2.5$ to $15 \mu\text{m}$) is specifically used for the finite-difference frequency-domain simulations of the next section; however, this range can be scaled linearly to any size.

For a system size in which the wavelength of the source light is much smaller than the gradient length scale of the scalar index profile, i.e., $\lambda \ll n/\|\nabla n\|$, a highly localized and highly directional light source, like a laser, would nearly approximate the geodesics of Eqs. (10) and (20). Simulating these trajectories amounts to ray tracing, which we pursue in Section 4.2. In particular, we explore the impact of imperfect construction and experimental error on the deviation of the ray trajectory from the geodesic. However, in the following section, we will first consider the case in which the source wavelength is *similar* to the size of the optical black hole, i.e., $\lambda/M \sim O(10)$. This is done to demonstrate the strengths and limitations of this study’s approach, as well as to be consistent with previous studies such as [28–30, 37, 41, 45, 46, 53].

4.1 Finite-difference frequency-domain simulations

In this section, the trajectory of light around an optical black hole is modeled using a finite-difference frequency-domain (FDFD) solver [54, 55] of Maxwell’s equations. The wavelength of light is chosen to be $\lambda = 0.5 \mu\text{m}$. The 2D simulation domain is modeled as a vacuum, with scalar properties $\epsilon = \mu = n = 1$ and size $60\lambda \times 60\lambda$; a perfectly matching layer of width $\lambda/5$ is applied at its boundary. A Gaussian beam

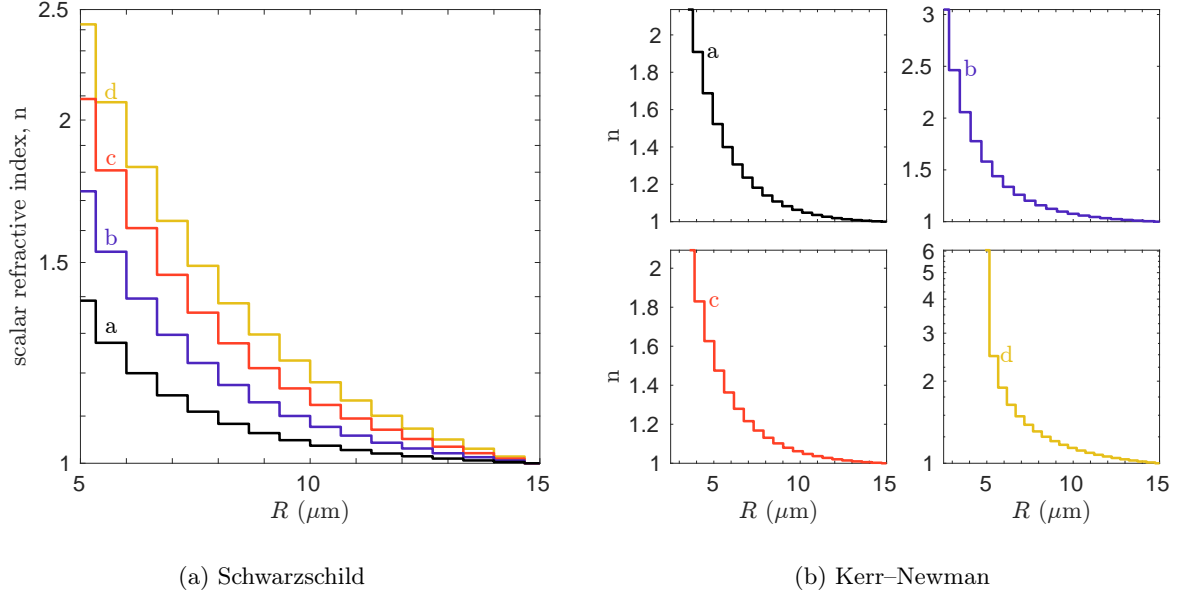


Figure 1: Radial profiles of the scalar refractive index used for simulations of optical (a) Schwarzschild and (b) Kerr–Newman black holes, shown in Figures 2 and 3, respectively. Labels a–d correspond to the profiles used in the respective subplots of Figures 2 and 3. The Schwarzschild radius for all simulations is $R_S = 5 \mu\text{m}$. Note the logarithmic scales and limits of the axes.

of light is approximated as an array of line sources, each of width 20 nm and amplitude calculated from a Gaussian envelope of the form $\exp(-(X - B_0)^2/2\delta^2)$, where B_0 is the real space impact parameter at P_0 and $\delta = \lambda/3$. The total width of the beam is truncated at 2λ by imposing two absorbing ($\epsilon = 1 - i\pi$) boundaries as vertically aligned “waveguides” of the light from the edge of the domain to the edge of the optical black hole; for example, see Figure 2. These restrict the beam to travel along a straight path in free space, as a directional light source would in the laboratory. Note that the factor of $-\pi$ is arbitrarily chosen for the imaginary (damping) component.

Each simulated optical black hole is centered in the domain, with the Schwarzschild radius always $R_S = 10\lambda = 5 \mu\text{m}$ ($M = 2.5 \mu\text{m}$) and edge at $R_0 = 30\lambda = 15 \mu\text{m}$. As seen in Figures 2 and 3, the Gaussian light source propagates in the vertical direction toward the black hole. Both minimum and maximum radii are shown as solid circles, while the edges of inner annuli are indicated by the small arcs. For all simulations, the region within the minimum radius (oftentimes the horizon radius R_h) is modeled as a disc with dielectric permittivity $\epsilon = \epsilon_{\text{in}} - i\pi$. Here, ϵ_{in} is the scalar permittivity ($\epsilon = n^2$) of the innermost annulus, and a factor of $-\pi$ is used for the imaginary (damping) component, as with the aforementioned “waveguides.”

4.1.1 Schwarzschild black holes

Figure 1(a) shows the profiles $n(R)$ used when modeling light incident on an optical Schwarzschild black hole with four different impact parameters, $\hat{b}_\infty = 2, 3, 4,$ and 5 ; the resulting FDFD simulations are shown in Figures 2(a) to 2(d), respectively.

Consider the simulation shown in Figure 2(a), for which the dedimensionalized impact parameter at infinity is $\hat{b}_\infty = 2$. The peak of the electric field normalized to its maximum, $|E|/\max|E|$, follows the path of the geodesic quite closely. Here, $|E| = \sqrt{E\bar{E}^*}$, with E^* the complex conjugate of E . The same spatial trend is seen in Figure 2(b), for which $\hat{b}_\infty = 3$. Note in Figure 1(a) how the profile of scalar index $n(R)$ increases in amplitude as the initial impact parameter increases, in order to further bend light toward the horizon. For $\hat{b}_\infty = 4$ and 5 , seen in Figures 2(c) and 2(d), respectively, the brightest regions of $|E|/\max|E|$ predominantly follow the geodesics. This is actually seen more clearly in the *energy* contained in the electric field ($\propto |E|^2$); however, only the electric field amplitude is shown here for better visualization of both small

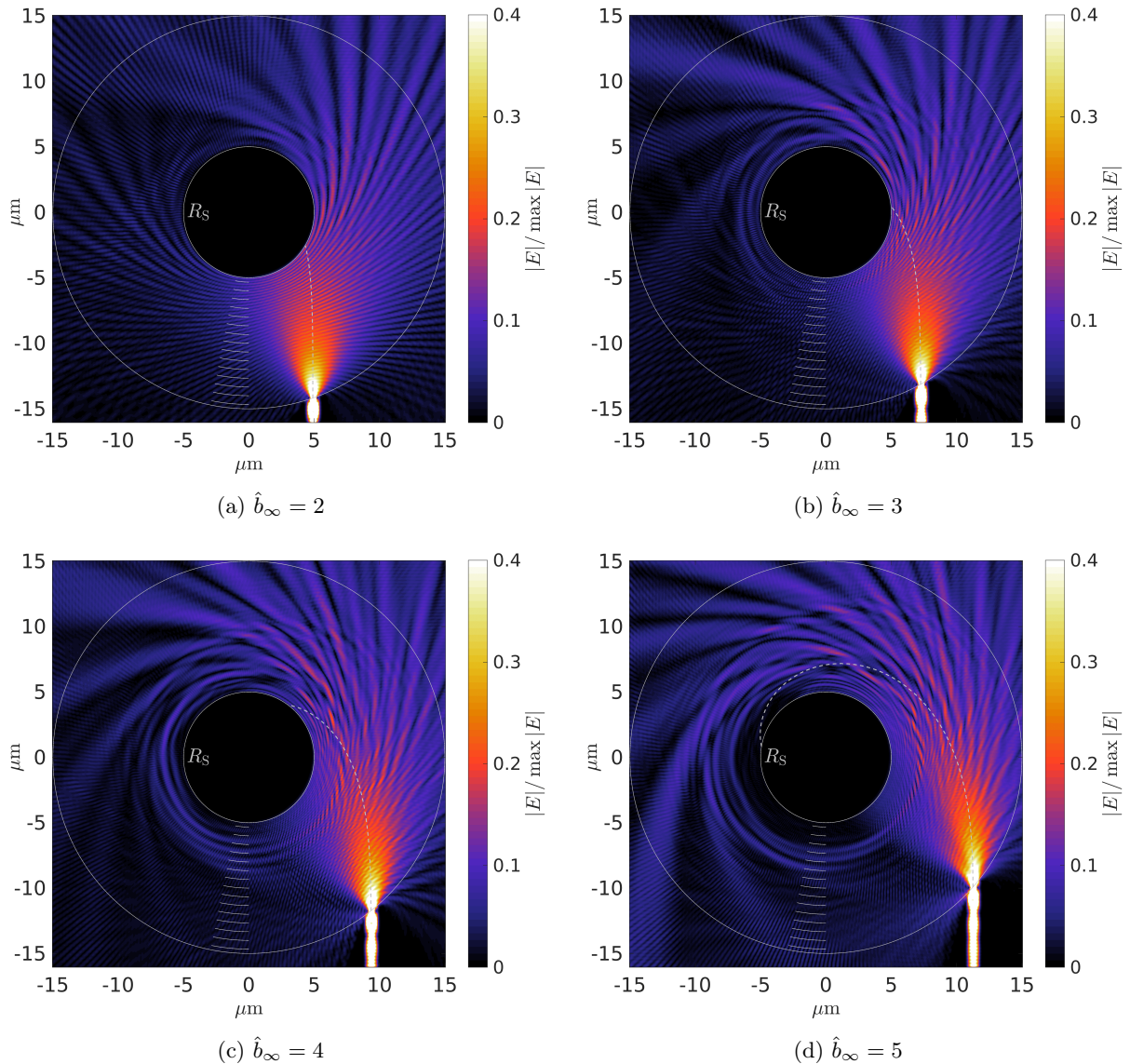


Figure 2: FDFD simulations of light incident on an optical Schwarzschild black hole with impact parameters $\hat{b}_\infty =$ (a) 2, (b) 3, (c) 4, and (d) 5. True geodesics are plotted as dashed lines. Initial and Schwarzschild radii are solid circles. Each interior annulus’s edge is marked; the accompanying profiles of scalar refractive index are given in [Figure 1\(a\)](#). Color scales for $|E|/\max|E|$ are the same for each subplot.

and large amplitude features. Agreement between the simulated light path and actual geodesic is expected to improve as the wavelength and beam width decrease relative to the size of the optical black hole, as described in [Section 4.2](#).

Another interesting effect is observed in [Figure 2\(d\)](#): the FDFD simulation does not show light following the geodesic all the way to the horizon. Instead, light begins to orbit at the photon sphere, $R = 3M = 7.5 \mu\text{m}$. This results because the impact parameter is nearly equal to that at which light becomes trapped, $\hat{b}_\infty = 3\sqrt{3} \approx 5.2$. Only traces of the photon “ring” are resolved in [Figure 2\(d\)](#). Higher fidelity simulations, with the optical black hole comprising many more annuli, would likely be required to properly simulate and study this phenomenon. This is left to future work.

4.1.2 Kerr–Newman black holes

Several optical Kerr–Newman black holes are also simulated, with profiles $n(R)$ in Figure 1(b) corresponding to the FDFD solutions in Figure 3. For each case, the impact parameter is $\hat{b}_\infty = 3$, and the outer edge of the optical black hole is again at radius $P_0 = 6$. These can be compared to the optical Schwarzschild black hole of Figure 2(b). The innermost modeled radius varies for each simulation, depending on whether $n(P)$ diverges outside of the horizon. Each simulation is described in detail below.

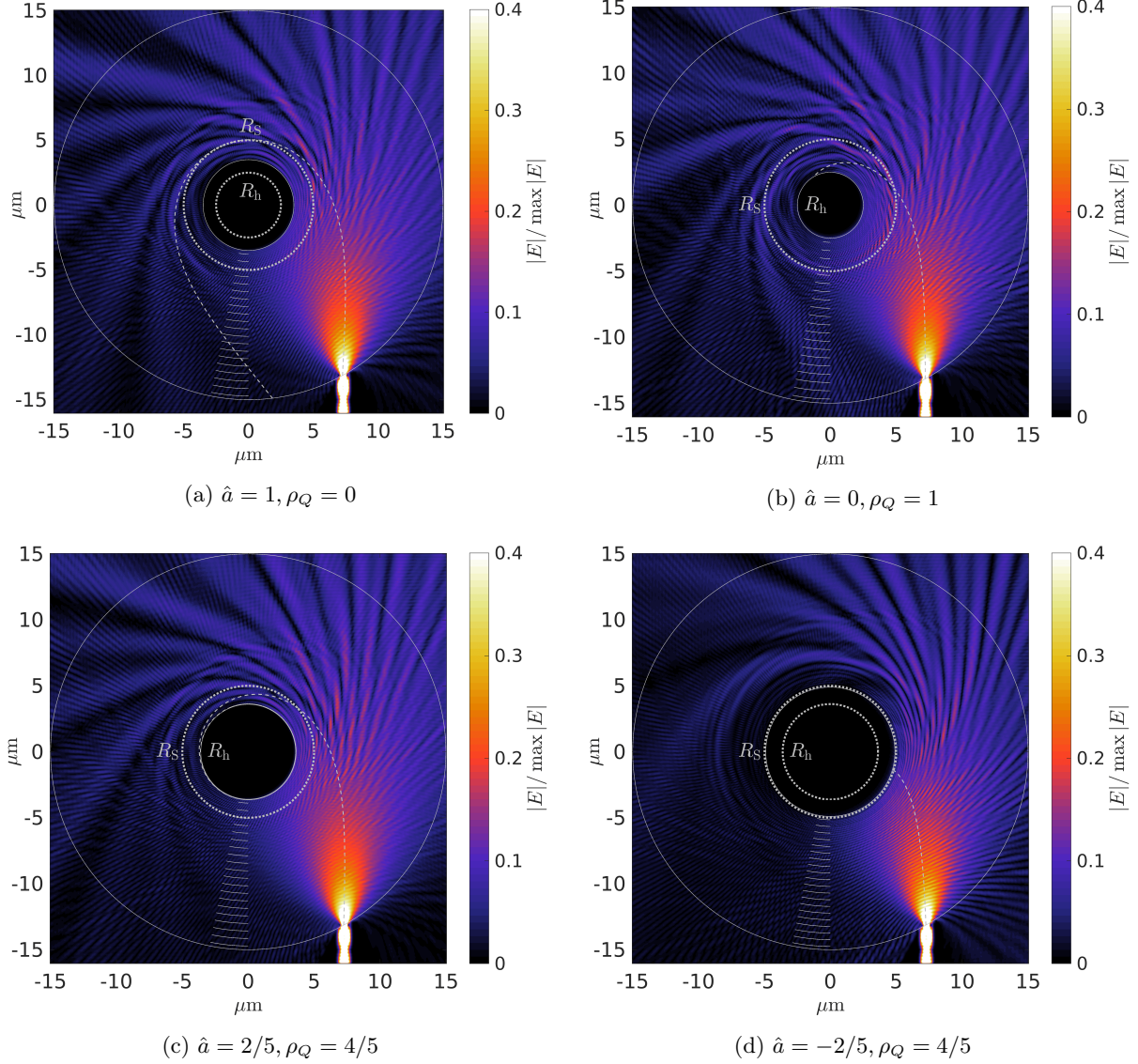


Figure 3: FDFD simulations of light incident ($\hat{b}_\infty = 3$) on four optical Kerr–Newman black holes, which are (a) maximally co-rotating ($\hat{a} = 1, \rho_Q = 0$); (b) maximally charged ($\hat{a} = 0, \rho_Q = 1$); (c) charged and co-rotating ($\hat{a} = 2/5, \rho_Q = 4/5$); and (d) charged and counter-rotating ($\hat{a} = -2/5, \rho_Q = 4/5$). True geodesics are plotted as dashed lines. Maximum and minimum radii are solid circles; radii of interest, such as the horizon or Schwarzschild radius, are also plotted and labeled. Each annulus' edge is marked; the accompanying profiles of scalar index are given in Figure 1(b). Color scales for $|E|/\max|E|$ are the same for each subplot. Compare to the simulation with $\hat{b}_\infty = 3, \hat{a} = 0, \rho_Q = 0$ in Figure 2(b).

An extremal Kerr black hole ($\hat{a} = 1, \rho_Q = 0$), with beam trajectory co-rotating with the black hole spin,

is shown in [Figure 3\(a\)](#). Here, $n(P)$ diverges at $P_* = 4/3$; however, the true geodesic escapes the black hole with $\frac{dr}{d\sigma} = 0$ at $P = 2$. Therefore, though the horizon is at $P_h = 1$, the system is modeled with innermost radius $P = 1.4$. Comparing to the Schwarzschild case in [Figure 2\(b\)](#), we see that light is “dragged” further around the co-rotating black hole, as expected. Additionally, more light “escapes,” although all is not directed along the geodesic.

In contrast to [Figure 3\(a\)](#), an extremal Reissner–Nordström black hole ($\hat{a} = 0, \rho_Q = 1$) is simulated, with FDFD results depicted in [Figure 3\(b\)](#). Here, the optical black hole could be modeled completely to the horizon at $R_h = 2.5 \mu\text{m}$. In general, the peak of $|E|/\max|E|$ follows the geodesic to the horizon. Little difference is seen when comparing to the Schwarzschild case of [Figure 2\(b\)](#), except that light now propagates within $R_S = 5 \mu\text{m}$.

Two non-extremal Kerr–Newman black holes, with the same charge ($\rho_Q = 4/5$) but opposite spins ($\hat{a} = \pm 2/5$), are also simulated and shown in [Figures 3\(c\)](#) and [3\(d\)](#). The *co-rotating* black hole is modeled to the horizon at $P_h = 1 + \sqrt{1/5} \approx 1.45$. Compared to the extremal Kerr black hole in [Figure 3\(a\)](#), light is not dragged as far around the black hole.

For the *counter-rotating* Kerr–Newman black hole, the profile $n(P)$ diverges at $P_* \approx 1.88$; this is the radius at which the geodesic begins co-rotating with the black hole spin, i.e., where $\frac{d\phi}{d\sigma} = 0$. Thus, the system is modeled only to $P = 1.96$, where $n(P = 1.96) \approx 6$. Comparing the co- and counter-rotating black holes, we see that light travels further in the Φ -direction for the former system, as expected.

As described in this section, a variety of optical Schwarzschild and Kerr–Newman black holes can be constructed feasibly with low indices of refraction. If such systems are built at a small scale, FDFD simulations show that the trajectories of light behave as expected, mostly following the true geodesics despite the discrete approximation to the proper gradient-index profile. The benefits of building larger systems are discussed in the next section.

4.2 Ray tracing calculations

In principle, the optical black holes of the previous section could be scaled in size from μm to cm or larger. This would simplify not only the construction of the optical black hole but also the calculation of light propagation, since the wavelength and width of the light source would be much smaller than the system size and related gradient length scales.

Consider again an optical system consisting of N concentric annuli. Let the radii bounding each annulus i be $R_i < R_{i-1}$, so that the annuli are numbered $1, 2, \dots, N$ from the outside in, and the outer edge of the system is at R_0 . The scalar index of each annulus is $n(R_i < R \leq R_{i-1}) = n_i$, which monotonically increases from annulus $1 \rightarrow N$, so $n_i < n_{i+1}$. Let the scalar index for $R > R_0$ be n_0 . For a light ray incident on annulus $(i + 1)$ (propagating in the region $R_i \leq R \leq R_{i-1}$), let the impact parameter be $B_i = R_i \sin \Phi_i$, where Φ_i is the azimuthal angle at which the ray intersects the annulus at R_i . Then, the azimuthal angle at which the light ray intersects the next annulus $(i + 2)$ at R_{i+1} is given by

$$\Phi_{i+1} - \Phi_i = \arcsin\left(\frac{B_{i+1}}{R_{i+1}}\right) - \arcsin\left(\frac{B_{i+1}}{R_i}\right), \quad (25)$$

provided that $B_{i+1} \leq R_{i+1}$. Note that the impact parameter always satisfies $n_i B_i = \text{constant}$. Thus, given an optical system with a well-defined profile $n(R)$ and an initial impact parameter B_0 , the trajectory of a light ray can be iteratively computed via [Eq. \(25\)](#) until the ray reaches its minimum radius. Note that only in-going trajectories are considered here, so light escaping the optical black hole is not modeled. Furthermore, it is assumed that all light is transmitted at each boundary; absorption and reflection are left for future work.

It is of interest to calculate the deviation of a ray trajectory around the optical black hole from the true geodesic. These deviations could occur for a number of reasons: for instance, the discretization of $n(R)$ due to the finite number of annuli; manufacturing error, leading to an offset Δn of the desired scalar index; or experimental error, resulting in a deviation ΔB_0 from the desired initial impact parameter B_0 . We explore the impacts of these below for light incident on an optical Schwarzschild black hole, with impact parameter $\hat{b}_\infty = 3$.

First, we consider the scenario in which the scalar index profile is imperfect, offset by a constant Δn due to some manufacturing error. The range of Δn spans $[0, 0.5]$ in [Figure 4](#); this is a significant percent change compared to profile b in [Figure 1\(a\)](#). At left in [Figure 4](#), we see that the ray trajectory skews radially

outward as Δn increases. The deviation of the ray trajectory from the geodesic is quantified by the difference in azimuthal angle, $\Delta\Phi = \Phi_{\text{ray}} - \Phi_{\text{geo}}$, as a function of radius, shown at right in Figure 4. Most trajectories follow the geodesic closely, within $\Delta\Phi \leq 2^\circ$, for $P > 3$; however, within $P < 3$, $\Delta\Phi$ grows rapidly. The small grey region, near $P \approx 2$ and $\Delta n \approx 0.5$, indicates that the ray trajectory escapes the black hole, so that $\Delta\Phi$ diverges. In this case, if errors of $\Delta\Phi \leq 5^\circ$ were allowable, then $n(R)$ must be constrained with $\Delta n \leq 0.1$.

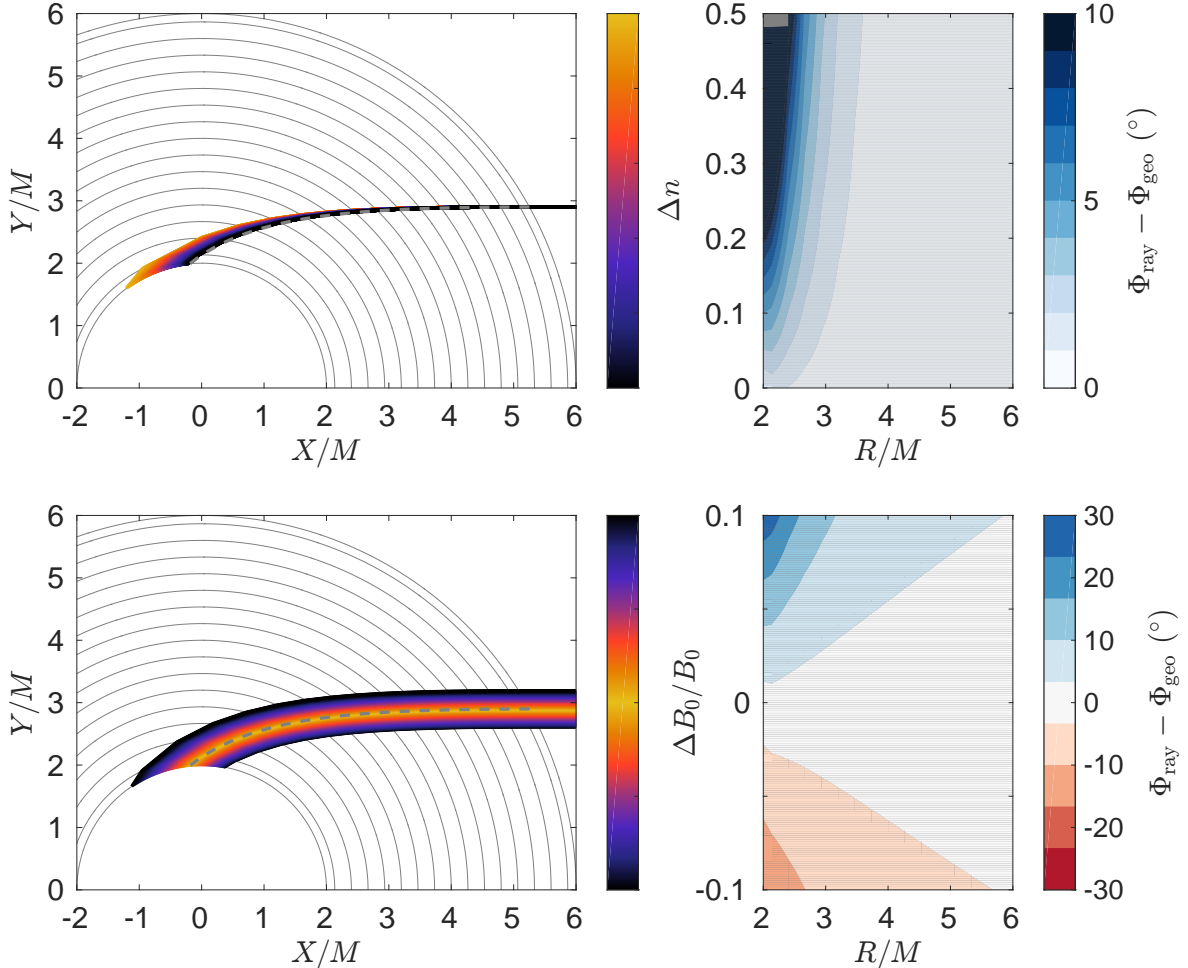


Figure 4: Effects of (top) a uniform offset Δn from the true scalar refractive index profile $n(R)$ and (bottom) a deviation ΔB_0 from the desired impact parameter B_0 . (Left) Ray trajectories in real space, computed from Eq. (25), compared to the true geodesic (grey dashed). (Right) Angular deviation of the rays from the geodesic versus radius. Both scans use the optical Schwarzschild black hole ($\hat{b}_\infty = 3$), shown in Figure 2(b) and with $n(R)$ given in Figure 1(a) as profile b. Each optical system (at left) has been rotated by $\pi/2$ for visualization purposes. Note that the scale of each colorbar on the plots *at left* is the same as the scale of the vertical axis on the plots *at right*.

In addition, a scan in initial impact parameter is performed to assess how experimental error would affect the ray trajectory. The ratio $\Delta B_0/B_0$ is varied within $\pm 10\%$, with results shown in Figure 4. The ray trajectories, at left, vary as expected: as $|\Delta B_0|$ increases, the ray path moves farther from the true geodesic, but keeps the same general shape. Again, the deviation in azimuthal angle is shown at right in Figure 4. For large $|\Delta B_0|/B_0$, $\Delta\Phi$ increases rapidly as the trajectory approaches the horizon. The deviation can be as large as $\Delta\Phi = 30^\circ$ at $P = 2$ when $\Delta B_0/B_0 \approx 10\%$.

Interestingly, the contours of $\Delta\Phi$ versus P and $\Delta B_0/B_0$ are not symmetric about $\Delta B_0/B_0 = 0$ in Figure 4. This results from the discretization of $n(R)$. Therefore, it could actually be beneficial to purposefully shift

the impact parameter in experiment ($\Delta B_0/B_0 < 0$, in this case) to better match the light trajectory with the true geodesic.

5 Conclusions

The application of transformation optics to studies of general relativity has seen a resurgence in theory, simulation, and experiment in the past two decades. Many recent works have focused on optical analogues to static, uncharged Schwarzschild black holes in an isotropic coordinate system. In this paper, we calculated the dielectric permittivity and permeability tensors ϵ, μ that exactly reproduce the metric of spinning, charged Kerr–Newman black holes. Furthermore, we conceived, for the first time, a gradient-index material that exactly reproduces families of equatorial Kerr–Newman null geodesics in almost all cases. Importantly, the radial profile of the scalar refractive index $n(R)$ is finite along the entire trajectory (even to the horizon, if applicable), except at the point of rotation reversal for initially counter-rotating null geodesics. Values of $n \lesssim 6$ can be achieved for many trajectories of interest, meaning that such gradient-index optical analogues could be constructed with conventional materials and metamaterials.

Simulations of a variety of optical black holes were performed, each with $n(R)$ approximated by concentric circular annuli of constant scalar index. First, a finite-difference frequency-domain (FDFD) solver of Maxwell’s equations was used to simulate the path of light incident on a Schwarzschild black hole with varying impact parameter $\hat{b}_\infty = b_\infty/M$. Good agreement was observed between the light trajectory (indicated by peaks of the electric field and electromagnetic energy) and geodesic for low impact parameters $\hat{b}_\infty = 2\text{--}3$, but the discrepancy grew for $\hat{b}_\infty = 4\text{--}5$. However, for $\hat{b}_\infty = 5$, some features of light orbiting at the photon sphere were observed.

Utilizing the same FDFD framework, several optical Kerr–Newman black holes were simulated: extremal Kerr, extremal Reissner–Nordström, and initially co- and counter-rotating trajectories. Each of these optical systems was simulated within the Schwarzschild radius, some even to the horizon. While there existed some discrepancies between the simulated light trajectories and true geodesics, the qualitative feature of light “dragged” in the direction of the black hole’s spin was observed. The three co-rotating cases require $n \lesssim 3$, meaning that constructions of these optical Kerr–Newman black holes are feasible; the counter-rotating case requires $n \lesssim 6$, which might be realized with metamaterials.

Finally, we investigated the effects of construction and experimental errors on these optical black holes, assuming the system size was large enough and source wavelength and beam were small enough to warrant ray tracing calculations. For the optical Schwarzschild black hole described and a chosen representative geodesic ($\hat{b}_\infty = 3$), a uniform increase in scalar index $\Delta n < 0.1$ could be tolerated with an angular difference between the modeled trajectory and geodesic $\Delta\Phi \leq 5^\circ$. Moreover, experimenters could be allowed an error in impact parameter $\Delta B_0/B$ within -6% to 4% while maintaining an angular deviation $\Delta\Phi \lesssim 10^\circ$.

Acknowledgements

This work grew from a submission to the Harvard Black Hole Initiative essay competition. The authors thank K. R. Moore for inspiration and R. Bekenstein, S. G. Johnson, N. Rivera, and S. P. Robinson for fruitful discussions. The authors also thank the MIT Department of Physics. A. Turner gratefully acknowledges the Tushar Shah and Sara Zion Fellowship for funding and was partially supported by DOE grant DE-SC00012567.

References

- [1] J. B. Pendry, D. Schurig, and D. R. Smith. Controlling electromagnetic fields. *Science*, 312(5781):1780–1782, 2006.
- [2] U. Leonhardt. Optical conformal mapping. *Science*, 312(5781):1777–1780, 2006.
- [3] U. Leonhardt. Notes on conformal invisibility devices. *New Journal of Physics*, 8(7):118, 2006.

- [4] D. Schurig, J. J. Mock, B. J. Justice, S. A. Cummer, J. B. Pendry, A. F. Starr, and D. R. Smith. Metamaterial electromagnetic cloak at microwave frequencies. *Science*, 314(5801):977–980, 2006.
- [5] W. Cai, U. K. Chettiar, A. V. Kildishev, and V. M. Shalaev. Optical cloaking with metamaterials. *Nature Photonics*, 1:224 EP –, 2007.
- [6] H. Chen, B.-I. Wu, B. Zhang, and J. A. Kong. Electromagnetic wave interactions with a metamaterial cloak. *Physical Review Letters*, 99:063903, 2007.
- [7] J. Li and J. B. Pendry. Hiding under the carpet: A new strategy for cloaking. *Physical Review Letters*, 101:203901, 2008.
- [8] D. R. Smith, J. B. Pendry, and M. C. K. Wiltshire. Metamaterials and negative refractive index. *Science*, 305(5685):788–792, 2004.
- [9] V. Veselago, L. Braginsky, V. Shklover, and C. Hafner. Negative refractive index materials. *Journal of Computational and Theoretical Nanoscience*, 3(2):189–218, 2006.
- [10] A. Grbic and G. V. Eleftheriades. Overcoming the diffraction limit with a planar left-handed transmission-line lens. *Physical Review Letters*, 92:117403, 2004.
- [11] N. Fang, H. Lee, C. Sun, and X. Zhang. Sub-wavelength diffraction-limited optical imaging with a silver superlens. *Science*, 308(5721):534–537, 2005.
- [12] H. Lee, Y. Xiong, N. Fang, W. Srituravanich, S. Durant, M. Ambati, C. Sun, and X. Zhang. Realization of optical superlens imaging below the diffraction limit. *New Journal of Physics*, 7:255–255, 2005.
- [13] D. O. S. Melville and R. J. Blaikie. Super-resolution imaging through a planar silver layer. *Optics Express*, 13(6):2127–2134, 2005.
- [14] U. Leonhardt and T. G. Philbin. General relativity in electrical engineering. *New Journal of Physics*, 8(10):247, 2006.
- [15] U. Leonhardt and T. G. Philbin. Chapter 2 Transformation Optics and the Geometry of Light. *Progress in Optics*, 53:69–152, 2009.
- [16] H. Chen, C. T. Chan, and P. Sheng. Transformation optics and metamaterials. *Nature Materials*, 9(5):387, 2010.
- [17] U. Leonhardt and T. Philbin. *Geometry and light: the science of invisibility*. Courier Corporation, 2010.
- [18] L. Xu and H. Chen. Conformal transformation optics. *Nature Photonics*, 9(1):15, 2015.
- [19] J. Plebanski. Electromagnetic waves in gravitational fields. *Physical Review*, 118:1396–1408, 1960.
- [20] F. de Felice. On the Gravitational field acting as an optical medium. *General Relativity and Gravitation*, 2:347, 1971.
- [21] B. Mashhoon. Scattering of electromagnetic radiation from a black hole. *Physical Review D*, 7:2807–2814, 1973.
- [22] M. O. Scully and W. Schleich. General Relativity And Modern Optics. In *Les Houches Summer School on Theoretical Physics: New Trends in Atomic Physics Les Houches, France, June 28-July 29, 1982*, pages 995–1124, 1982.
- [23] R. T. Thompson and J. Frauendiener. Dielectric analog space-times. *Physical Review D*, 82:124021, 2010.
- [24] B. Reznik. Origin of the thermal radiation in a solid-state analogue of a black hole. *Physical Review D*, 62:044044, 2000.

- [25] R. Schützhold, G. Plunien, and G. Soff. Dielectric black hole analogs. *Physical Review Letters*, 88:061101, 2002.
- [26] W. G. Unruh and R. Schützhold. On slow light as a black hole analogue. *Physical Review D*, 68:024008, 2003.
- [27] A. Greenleaf, Y. Kurylev, M. Lassas, and G. Uhlmann. Electromagnetic wormholes and virtual magnetic monopoles from metamaterials. *Physical Review Letters*, 99:183901, 2007.
- [28] D. A. Genov, S. Zhang, and X. Zhang. Mimicking celestial mechanics in metamaterials. *Nature Physics*, 5:687, 2009.
- [29] E. E. Narimanov and A. V. Kildishev. Optical black hole: Broadband omnidirectional light absorber. *Applied Physics Letters*, 95(4):041106, 2009.
- [30] Q. Cheng, T. J. Cui, W. X. Jiang, and B. G. Cai. An omnidirectional electromagnetic absorber made of metamaterials. *New Journal of Physics*, 12(6):063006, 2010.
- [31] M. Li, R.-X. Miao, and Y. Pang. Casimir energy, holographic dark energy and electromagnetic metamaterial mimicking de sitter. *Physics Letters B*, 689(2):55 – 59, 2010.
- [32] I. I. Smolyaninov. Metamaterial ‘multiverse’. *Journal of Optics*, 13(2):024004, 2010.
- [33] T. G. Mackay and A. Lakhtakia. Towards a metamaterial simulation of a spinning cosmic string. *Physics Letters A*, 374(23):2305 – 2308, 2010.
- [34] T. H. Anderson, T. G. Mackay, and A. Lakhtakia. Ray trajectories for a spinning cosmic string and a manifestation of self-cloaking. *Physics Letters A*, 374(46):4637 – 4641, 2010.
- [35] T. G. Mackay and A. Lakhtakia. Towards a realization of Schwarzschild-(anti-)de Sitter spacetime as a particulate metamaterial. *Physical Review B*, 83:195424, 2011.
- [36] I. I. Smolyaninov and Y.-J. Hung. Modeling of time with metamaterials. *Journal of the Optical Society of America B*, 28(7):1591–1595, 2011.
- [37] H.-W. Wang and L.-W. Chen. A cylindrical optical black hole using graded index photonic crystals. *Journal of Applied Physics*, 109(10):103104, 2011.
- [38] I. I. Smolyaninov, Y.-J. Hung, and E. Hwang. Experimental modeling of cosmological inflation with metamaterials. *Physics Letters A*, 376(38):2575 – 2579, 2012.
- [39] Y. Yang, L. Y. Leng, N. Wang, Y. Ma, and C. K. Ong. Electromagnetic field attractor made of gradient index metamaterials. *Journal of the Optical Society of America A*, 29(4):473–475, 2012.
- [40] M. Yin, X. Yong T., L. L. Wu, and D. C. Li. A broadband and omnidirectional electromagnetic wave concentrator with gradient woodpile structure. *Optics Express*, 21(16):19082–19090, 2013.
- [41] C. Sheng, H. Liu, Y. Wang, S. N. Zhu, and D. A. Genov. Trapping light by mimicking gravitational lensing. *Nature Photonics*, 7:902 EP –, 2013. Article.
- [42] R. Bekenstein, R. Schley, M. Mutzafi, C. Rotschild, and M. Segev. Optical simulations of gravitational effects in the Newton-Schrödinger system. *Nature Physics*, 11:872 EP, 2015.
- [43] A. Patsyk, M. A. Bandres, R. Bekenstein, and M. Segev. Observation of accelerating wave packets in curved space. *Physical Review X*, 8:011001, 2018.
- [44] U. Leonhardt. Quantum physics of simple optical instruments. *Reports on Progress in Physics*, 66(7):1207–1249, 2003.
- [45] H. Chen, R.-X. Miao, and M. Li. Transformation optics that mimics the system outside a Schwarzschild black hole. *Optics Express*, 18(14):15183–15188, 2010.

- [46] I. Fernández-Núñez and O. Bulashenko. Anisotropic metamaterial as an analogue of a black hole. *Physics Letters A*, 380(1):1 – 8, 2016.
- [47] R. Bekenstein, Y. Kabessa, Y. Sharabi, O. Tal, N. Engheta, G. Eisenstein, A. J. Agranat, and M. Segev. Control of light by curved space in nanophotonic structures. *Nature Photonics*, 11(10):664–670, 2017.
- [48] X.-H. Ye and Q. Lin. Gravitational lensing analyzed by the graded refractive index of a vacuum. *Journal of Optics A: Pure and Applied Optics*, A10:1–6, 2008.
- [49] Steven Weinberg. *Gravitation and Cosmology: Principles and Applications of the General Theory of Relativity*. Wiley, New York, NY, 1972.
- [50] D. Christodoulou and R. Ruffini. Reversible transformations of a charged black hole. *Physical Review D*, 4:3552–3555, Dec 1971.
- [51] R. T. Thompson, S. A. Cummer, and J. Frauendiener. A completely covariant approach to transformation optics. *Journal of Optics*, 13(2):024008, 2010.
- [52] R. T. Thompson, S. A. Cummer, and J. Frauendiener. Generalized transformation optics of linear materials. *Journal of Optics*, 13(5):055105, 2011.
- [53] W. Lu, J. Jin, Z. Lin, and H. Chen. A simple design of an artificial electromagnetic black hole. *Journal of Applied Physics*, 108(6):064517, 2010.
- [54] W. Shin and S. Fan. Choice of the perfectly matched layer boundary condition for frequency-domain Maxwell’s equations solvers. *Journal of Computational Physics*, 231(8):3406 – 3431, 2012.
- [55] Wonseok Shin. MaxwellFDFD Webpage, 2015. <https://github.com/wsshin/maxwelldfd>.